

Fine Tuning Electronic Structure of Catalysts through Atomic Engineering for Enhanced Hydrogen Evolution

Yichao Huang, Jun Hu, Haoxiang Xu, Wei Bian, Jingxuan Ge, Dejin Zang, Daojian Cheng,* Yaokang Lv, Cheng Zhang,* Jing Gu,* and Yongge Wei*

An efficient, durable, and low-cost hydrogen evolution reaction (HER) catalyst is an essential requirement for practical hydrogen production. Herein, an effective approach to facilitate the HER kinetics of molybdenum carbide (Mo_2C) electrocatalysts is presented by tuning its electronic structure through atomic engineering of nitrogen implantation. Starting from the organoimido-derivatized polyoxometalate nanoclusters with inherent Mo–N bonds, the formation of N-implanted Mo_2C ($\text{N@Mo}_2\text{C}$) nanocrystals with perfectly adjustable amounts of N atoms is demonstrated. The optimized $\text{N@Mo}_2\text{C}$ electrocatalyst exhibits remarkable HER performance and good stability over 20 h in both acid and basic electrolytes. Further density functional theory calculations show that engineering suitable nitrogen atoms into Mo_2C can regulate its electronic structure well and decrease Mo–H strength, leading to a great enhancement of the HER activity. It could be believed that this ligand-controlled atomic engineering strategy might influence the overall catalyst design strategy for engineering the activation sites of nonprecious metal catalysts for energy conversions.

1. Introduction

Hydrogen is an environmentally friendly energy carrier with a great potential to reduce our energy dependence on fossil fuels due to its high energy density and sustainability.^[1–3] However, the production of hydrogen by the traditional gasification of coal or steam-methane reforming causes a significant increase in the emission of carbon dioxide, inducing detrimental climate change.^[4,5] The direct electrochemical splitting of water has been considered to be an attractive alternative pathway to produce hydrogen.^[6,7] Yet, the large energy input validated by overpotential of the hydrogen evolution reaction (HER) greatly limited the practical utilization of the overall water splitting.^[8–10] Furthermore, the state-of-the-art electrocatalysts for HER are Pt-based materials, but their high cost and scarcity seriously impede their large-scale applications in


electrocatalytic HER.^[11] To overcome these disadvantages, great efforts have been devoted to developing non-noble catalysts with highly efficient and stable HER catalytic activities,^[12] including alloy,^[13] transition-metal (TM) borides,^[14,15] carbides,^[16–20] nitrides,^[20,21] oxides,^[22] phosphides,^[6,23–25] and sulfides.^[7,26–30] Among these catalysts, molybdenum carbide (Mo_2C) has drawn considerable attention since its electronic structure closely resembles that of platinum.^[20,31–40] The HER activity of Mo_2C was first studied by Hu's group in 2012, which was convinced to be a promising catalyst for HER in both acidic and basic conditions.^[36] However, further, it was demonstrated that the intrinsic HER activity of Mo_2C is usually limited by their large density of empty d-orbitals on the Mo, which restricts the desorption of adsorbed H (H_{ads}) to generate H_2 .^[41,42] Introducing electron-rich dopants, such as N (3.06), to downshift the density of empty d-bands in Mo_2C is a variable approach to reduce Mo–H bond strength, enhancing its HER activity.^[43] However, nitrogen-doping (N-doping) often intermixes into carbon matrix rather than intercalating into Mo_2C active sites,^[16,44–48] and thus how to construct a controllable N-doping into Mo_2C activation site still remains a great challenge. It should be noted that using NH_3 as an N source, as in the previously reported strategy, is very limited since this doping strategy is uncontrolled, in which most of the N-doping happen only on the surface in a gas–solid diffusion reaction.^[21,49] Additionally, other

Y. C. Huang, J. Hu, W. Bian, J. X. Ge, Dr. D. J. Zang, Prof. Y. G. Wei
Key Lab of Organic Optoelectronics & Molecular Engineering of
Ministry of Education
Department of Chemistry
Tsinghua University
Beijing 100084, P. R. China
E-mail: yonggewei@mail.tsinghua.edu.cn

Y. C. Huang, Prof. J. Gu
Department of Chemistry and Biochemistry
San Diego State University
5500 Campanile Drive, San Diego, CA 92182-1030, USA
E-mail: jgu@sdsu.edu

H. X. Xu, Prof. D. J. Cheng
International Research Center for Soft Matter
Beijing Key Laboratory of Energy Environmental Catalysis
State Key Laboratory of Organic–Inorganic Composites
Beijing University of Chemical Technology
Beijing 100029, P. R. China
E-mail: chengdj@mail.buct.edu.cn

Dr. Y. K. Lv, Prof. C. Zhang
College of Chemical Engineering and Materials Science
Zhejiang University of Technology
Hangzhou 310014, P. R. China
E-mail: czhang@zjut.edu.cn

 The ORCID identification number(s) for the author(s) of this article can be found under <https://doi.org/10.1002/aenm.201800789>.

DOI: 10.1002/aenm.201800789

strategies based on mixing N-containing organic compounds (such as dicyandiamide,^[45] polypyrrole,^[47] or melamine^[48]) also suffer from difficulties including unpredictably controlling the dopants concentration and doping sites. In most of these cases, the N atoms tend to intercalate into carbon supports rather than the Mo₂C, leading to negligible electronic property regulation on Mo₂C, resulting the structure–activity relationship of N-doped Mo₂C remains ambiguous. Therefore, it is of great significance to develop an effective protocol to control the N-doping in Mo₂C active phase and further exam into the N-doping concentration effect on the electrochemical performance of Mo₂C catalysts.

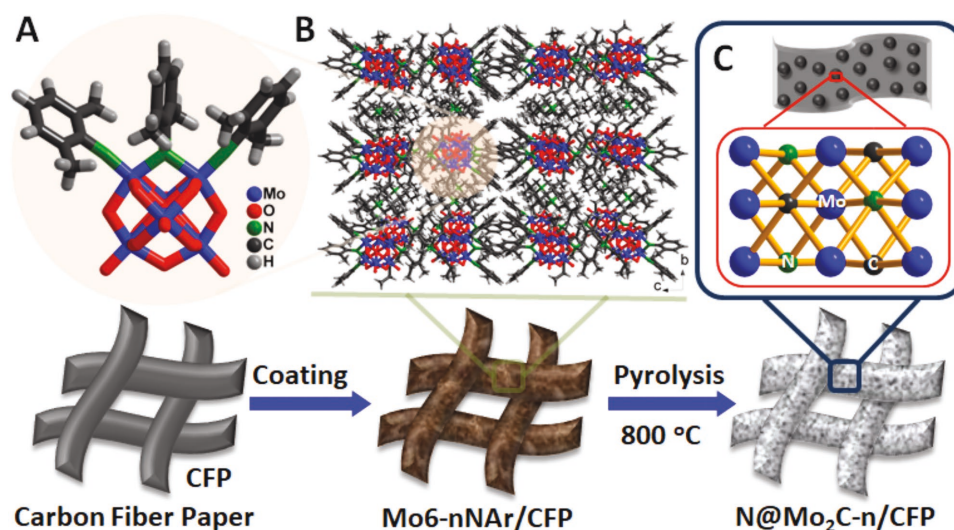
Polyoxometalates (POMs) are a special class of metal oxide anion clusters with well-defined molecular nanostructures.^[50–53] Covalently incorporating functional organic moieties in a controllable manner onto the POMs surfaces make the precursor structure versatility more accessible. Our previous works have shown that the organoimido-derivatized hexamolybdates [Mo₆O₁₉]²⁻ (Mo6, a typical Lindqvist-type POM) can be easily acquired by applying various N-containing arylamine ligands to replace oxo sites in Mo6 clusters, which reconcile the quantitative amount of Mo–N bonds.^[54–56] Recent work by our group has demonstrated that organoimido-derivatized POM clusters with arylamine ligands and phenylphosphonic acid ligands can function as the molybdenum, carbon, nitrogen, and phosphorus sources, and in situ carbonization will result in the formation of Mo₂C and MoP hybrids.^[57] Herein, we propose that the amount of nitrogen incorporations into Mo₂C structure could be well controlled by using various organoimido-derivatized POMs with inherent Mo–N bonds as precursors (Scheme 1). Moreover, another advantage of using organoimido-derivatized POMs as the precursor is that less agglomeration of the Mo₂C particles could be achieved by the structure-induced confinement of arylimido ligands and well-dispersed tetrabutyl ammonium (TBA) ions. Although the Keggin-type POMs cluster, [PMo₁₂O₄₀]³⁻, and their MOFs composites, have been reported

to serve as precursors for Mo₂C electrocatalysts,^[21,40,46] such a ligand-controlled atomic engineering strategy via the design of various covalently organoimido-functionalized POMs structure frameworks has not yet been reported. In this work, controllable atomic engineering of nitrogen implantation into porous Mo₂C nanocrystal has been achieved through a facile pyrolysis of various organoimido-derivatized POMs (Mo6-*n*NAr) on a carbon fiber paper (CFP), a widely used conductive support.^[58,59] The combined theoretical density functional theory (DFT) calculations and experimental results demonstrated that the sluggish HER kinetics of Mo₂C catalysts could be significantly improved through engineering N atoms due to the fine tuning of the electronic structure on Mo₂C, leading to suitable Mo–H binding strength and remarkable HER performance.

2. Results and Discussion

2.1. Synthesis and Characterization of Catalysts

First, a series of organoimido-derivatized POM precursors with different amounts of arylimido ligands, (TBA)₂[Mo₆O_{19–*n*}(NAr)_{*n*}] (denoted as Mo6-*n*NAr; *n* referring to the number of Mo–N bonds in Mo6-*n*NAr precursors; Ar = 2,6-Me₂-phenyl) were designed and synthesized by the well-developed dicyclohexylcarbodiimide (DCC)-dehydrating protocol.^[54,60,61] The purity of the abovementioned precursors was confirmed by infrared spectroscopy (IR), elemental analysis (EA), and electron spray ionization mass spectrometry (ESI-MS) (Figures S1 and S2, Supporting Information). As illustrated in Scheme 1, different Mo6-*n*NAr precursors were then coated on CFP forming Mo6-*n*NAr/CFP composites (Figures S3 and S4, Supporting Information). The as-prepared Mo6-*n*NAr/CFP composites were then pyrolyzed under an argon gas atmosphere at 800 °C for 3 h to obtain the targeted N@Mo₂C-*n*/CFP materials with varied N-doping.



Scheme 1. Schematic illustration of the synthesis of N-implanted porous nanostructured Mo₂C electrocatalysts on the carbon fiber paper, N@Mo₂C-*n*/CFP. Taking N@Mo₂C-3/CFP for example, the A) Mo6-3NAr precursors were first coated on the surface of CFP forming B) Mo6-3NAr/CFP composites, which were then pyrolyzed under argon gas atmosphere at 800 °C for 3 h, forming the C) targeted N@Mo₂C-3/CFP materials. Color code: blue, Mo; black, C; green, N.

After annealing at 800 °C for 3 h, N@Mo₂C-3/CFP, demonstrated here as a representative for other N@Mo₂C-*n*/CFP, was obtained and its morphology changed from an original smooth (Figure 1A) morphology into a rough layer decorated with uniform nanoparticles (Figure 1B), similar to those of N@Mo₂C-0/CFP, N@Mo₂C-1/CFP, N@Mo₂C-2/CFP, and N@Mo₂C-5/CFP (Figure S5, Supporting Information). Interestingly, the layer structure of Mo₆-3NAr precursor is well retained in N@Mo₂C-3/CFP (Figure 1C). Transmission electron microscopy (TEM) imaging on the as-obtained N@Mo₂C-3 nanosheet layer shows that numerous nanoparticles with a size of ≈15 nm are well embedded in the porous nanosheet. The crystalline structure of the N@Mo₂C-3 nanosheet was studied by powder X-ray diffraction (PXRD, light blue curve in Figure 1D), which clearly displayed the characteristic diffraction peaks at 34.4°, 38.0°, and 39.4°, corresponding to the (0 2 1), (2 0 0), and (1 2 1) planes of an orthorhombic Mo₂C (PDF#79-0744). The high-resolution TEM (HRTEM) image clearly discloses that nanosheet layer of N@Mo₂C-3 is composed of well-crystallized

nanoparticles on the amorphous carbon matrix (Figure 1E). The apparent lattice fringes on the nanoparticles with distances of 0.26, 0.24, and 0.23 nm could be attributed to (0 2 1), (2 0 0), and (1 2 1) crystallographic planes of orthorhombic Mo₂C, in agreement with the PXRD results. Similar XRD patterns have been observed for the other N@Mo₂C-*n* nanosheets, indicating their similar crystalline structures (Figure 1E). Meanwhile, diffraction peaks at 26.4° and 54.5° for N@Mo₂C-*n*/CFP catalysts could be assigned to (1 1 1) and (2 2 2) planes of graphite carbon (PDF#75-0444) derived from CFP (Figure S6, Supporting Information). Moreover, the uniform distribution of Mo, C, and N elements in N@Mo₂C-3 has been illustrated by energy dispersive X-ray (EDX) elemental mappings (Figure 1F; Figure S5, Supporting Information), further confirming that the nanoparticles are constituted by molybdenum, carbon, and nitrogen species. The contents of Mo, C, and N of various N@Mo₂C-*n* layers without CFP are also calculated via the EDX and EA, respectively, which are summarized in Table S1a (Supporting Information). As expected, the N contents of N@Mo₂C-*n* are increased with the increase of the *n* value. The presence of amorphous carbon in N@Mo₂C-*n* nanosheets without CFP can be verified by thermal gravimetric analysis (TGA) and Raman spectrum (Figures S7 and S8, Supporting Information), which is believed to play an important role in prohibiting the aggregation of Mo₂C nanoparticles and stabilizing the nanosheet structures. The porous property of N@Mo₂C-3 nanosheet is revealed by N₂ adsorption–desorption isotherm measurements (Figure S9, Supporting Information). Meanwhile, the specific surface areas and pore sizes of the N@Mo₂C-3 nanosheet layer are measured by the Brunauer–Emmett–Teller (BET) and the Barrett–Joyner–Hallender methods, exhibiting a high specific BET surface area of 180.31 m² g⁻¹ and an average pore size of 3.7 nm (Table S1a, Supporting Information).

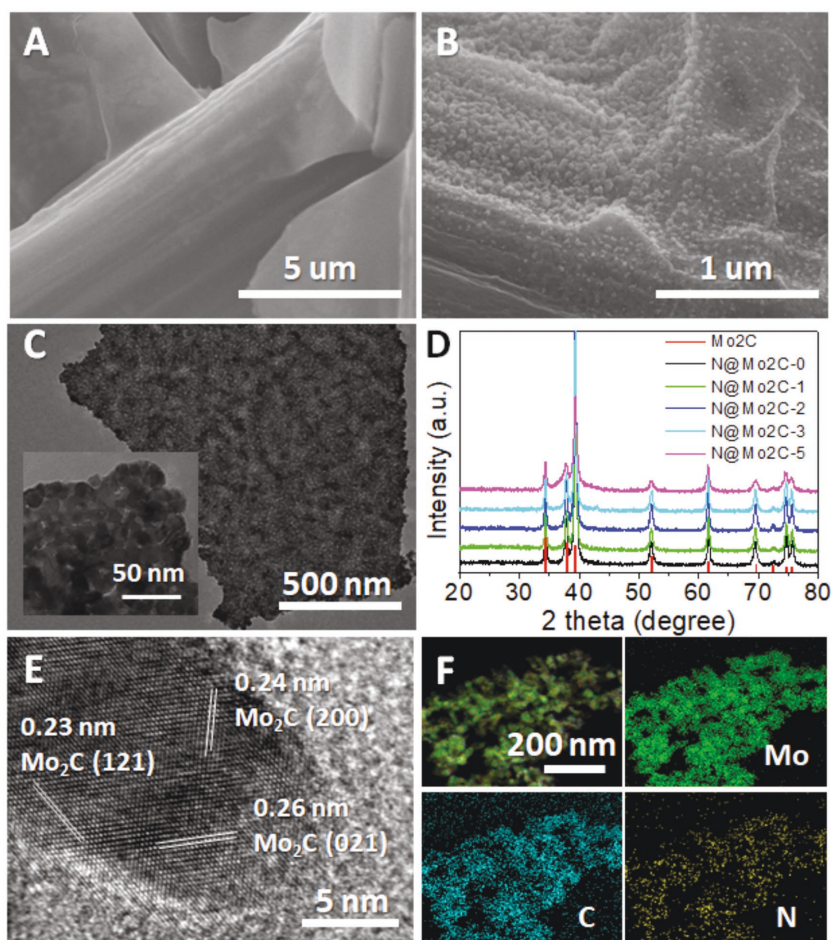


Figure 1. The characterizations of the Mo₆-3NAr/CFP composite and the as-prepared N@Mo₂C-3/CFP catalyst. A) SEM image of the Mo₆-3NAr/CFP composite (scale bar, 5 μm). B) SEM images of the as-prepared N@Mo₂C-3/CFP (scale bar, 1 μm). C) TEM image of porous N@Mo₂C-3 nanosheet catalyst peeled from N@Mo₂C-3/CFP (scale bar, 500 nm). D) Powder X-ray diffraction patterns of N@Mo₂C-*n*/CFP materials (red, β-Mo₂C-PDF#79-0744). E) HRTEM image of N@Mo₂C-3 catalyst (scale bar, 5 nm). F) Elemental mapping of porous N@Mo₂C-3 catalyst (scale bar, 200 nm).

2.2. Fine Tuning Electronic Structures of Catalysts

The efficient regulation of electronic structure of N@Mo₂C-*n* catalysts was proved by X-ray photoelectron spectroscopy (XPS) (Figure 2). The chemical composition and the valence state of N@Mo₂C-3 were first tested by XPS measurement. As shown in Figure 2A, the XPS spectrum of N@Mo₂C-3 indicated the presence of Mo, C, and N elements. The high-resolution Mo 3d spectrum was deconvoluted into eight peaks (Figure 2B). The peaks located at 232.0 and 228.7 eV verify the formation of Mo–N species.^[44–47] The peaks at 231.3 and 228.1 eV are attributed to Mo–C bond from Mo₂C.^[21,49] The peaks located at higher binding energy

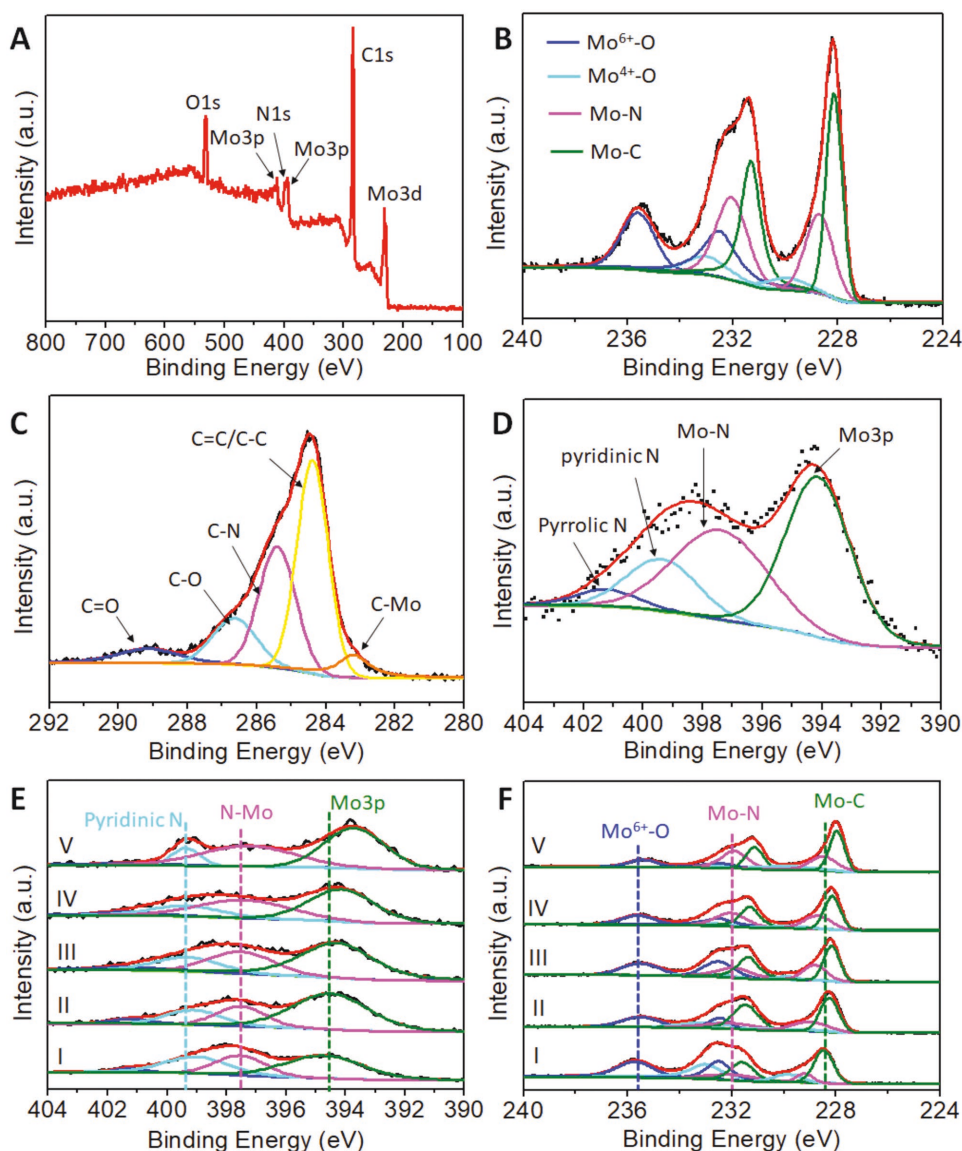


Figure 2. XPS spectra of N@Mo₂C-*n* catalysts. A) Wide-scan survey XPS spectrum of N@Mo₂C-3 nanosheet layer. High-resolution XPS signals of B) Mo3d, C) C 1s and D) N 1s for N@Mo₂C-3 nanosheet layer. XPS signals of N@Mo₂C-*n* layer, including E) the N 1s signals and F) the Mo 3d signals of N@Mo₂C-0 (I), N@Mo₂C-1 (II), N@Mo₂C-2 (III), N@Mo₂C-3 (IV), and N@Mo₂C-5 (V).

correspond to Mo⁶⁺ (235.5 and 232.5 eV) and Mo⁴⁺ (233.0 and 229.9 eV), which can be assigned to MoO₃ and MoO₂ possibly from the surface oxidation of Mo species, which is commonly present in the other Mo catalysts.^[36–40] The main peak located at 284.34 eV can be attributed to the graphite carbon matrix (Figure 2C), which corresponds well with the above Raman results (Figure S8, Supporting Information). The peak around 285.23 eV can be ascribed to the peak of carbon in C–N bonds, which should be attributed to the N-doping in carbon matrix during the pyrolysis at high temperature. The small shoulder at about 283 eV can be attributed to C 1s of Mo₂C according to the NIST database and the reported literature.^[62,63] The N peaks located at 399.4 eV may be ascribed to the pyridinic N while the peak at 397.4 eV can be assigned to the Mo–N bonds, perfectly serving as the second evidence for the successful N-doping in

Mo₂C (Figure 2D).^[21] The above XPS analyses demonstrate the possible N-doping in both Mo₂C and the carbon matrix. Thus, we may declare that the N@Mo₂C-3 nanosheet layer is composed of N-doped Mo₂C nanocrystals and a porous N-doped carbon matrix.

Since Mo²⁺ and Mo³⁺ oxidation states are believed to be the catalytic active states for electrocatalytic HER, the influence of N-doping on their binding energies was discussed in more detail.^[16–21] Also, the binding energy of Mo⁶⁺ (Mo 3d_{5/2}: 232.5 eV, 3d_{3/2}: 235.5 eV) and Mo⁴⁺ (Mo 3d_{5/2}: 229.9 eV; 3d_{3/2}: 233.0 eV) does not change much and is consistent with the literature values.^[36–40] Compared between all N@Mo₂C-*n* catalysts, the intensity of N 1s (N–Mo, N 1s: 397.5 eV) and Mo³⁺ (Mo–N, Mo 3d_{3/2}: 232.0 eV) peaks is increased with the increased amount of N dopants (Figure 2E,F). With the

increase of N dopants, the pyridinic N (C–N N 1s: 399.1 eV) peak only slightly shifts to a higher binding energy (399.3 eV), indicating the amounts of N dopants have little influence on the electronic structure of the carbon matrix. In the contrary, Mo 3p peaks binding energy displays an obvious downward shift from 394.7 eV to 393.7 eV with a rise of N intercalating amounts in all N@Mo₂C-*n* catalysts (Figure 2E). Similar downshifts of binding energies for Mo²⁺ (Mo–C, Mo 3d_{5/2}) are also observed (Figure 2F). Simultaneously, the peak of Mo 3d_{5/2} in Mo₂C is located at 228.8 eV, according to the NIST database and the previous reports.^[62,64] As shown in Figure 2F, the peak for Mo²⁺ (Mo 3d_{5/2}) is visibly downshifted from 228.5 eV to 228.0 eV with an increased amount of N dopants in N@Mo₂C-*n* catalysts (Table S1b, Supporting Information), indicating the electronic structure of Mo atoms in Mo₂C can be well regulated by N-doping.^[65] The above results further corroborate that fine tuning the magnitude of the derivative organoimido ligands in POM precursors could assist the regulation of the number of intercalated N atoms in Mo₂C electrocatalysts.

2.3. Evaluation of Electrochemical HER Activities

The HER performance of N@Mo₂C-*n*/CFP electrocatalysts was evaluated in both acidic (0.5 M H₂SO₄) and basic (1 M KOH) conditions. 20% Pt/C (Johnson Matthey) was also measured for comparison purposes (Figure 3). Remarkably, an obvious enhancement of HER activity is observed after using POMs precursors with inherent Mo–N bonds (Figure 3A,C). Moreover, N@Mo₂C-3/CFP presents the highest HER activity among the N@Mo₂C-*n*/CFP electrocatalysts, superior to most of the Mo-based HER catalysts (Tables S3 and S4, Supporting Information). This result indicates that the HER activity of Mo₂C electrocatalyst can be significantly improved by the engineering of suitable N atoms into Mo₂C. In acidic condition, to drive a current density of 10 mA cm⁻², N@Mo₂C-3/CFP only needs an overpotential (η) of 56 mV (Figure 3B). The HER performances of the as-prepared N@Mo₂C-*n*/CFP electrocatalysts were also investigated in alkaline conditions (1 M KOH). The N@Mo₂C-3/CFP also exhibits remarkable electrocatalytic HER performance (Figure 3C). As shown in Figure 3D, only a small overpotential of 66 mV is needed to afford a current density of 10 mA cm⁻² for the N@Mo₂C-3/CFP electrocatalyst, which is superior to the other N@Mo₂C-*n*/CFP as well as most of the reported Mo-based electrocatalysts, as shown in Table S4 (Supporting Information). Interestingly, we noticed that the cathodic current of the N@Mo₂C-3/CFP catalyst exceeds that of Pt/C when the potential is lower than –117 mV (Figure 3C).

The HER kinetics of N@Mo₂C-*n*/CFP catalysts were further evaluated by Tafel plots. As shown in Figure 3E, N@Mo₂C-3/CFP catalyst shows a Tafel slope of 51 mA dec⁻¹ in 0.5 M H₂SO₄ media, close to 20% Pt/C (32 mA dec⁻¹) and smaller than the other N@Mo₂C-*n*/CFP, corresponding well with the overpotential results. In 1 M KOH electrolyte, the Tafel slope of N@Mo₂C-3/CFP (49 mA dec⁻¹) was also demonstrated to be smaller than those of N@Mo₂C-0/CFP (98 mA dec⁻¹), N@Mo₂C-1/CFP (72 mA dec⁻¹), N@Mo₂C-2/CFP (53 mA dec⁻¹), and @Mo₂C-5/CFP (65 mA dec⁻¹) (Figure 3F). It has been reported that the HER proceeds in an acidic media via two steps, including

the H⁺ electrochemical reduction step (Volmer reaction with a Tafel slope of 118 mV dec⁻¹) and the H_{ads} desorption step (Heyrovsky process with a slope of 40 mV dec⁻¹ or Tafel process with a slope of 30 mV dec⁻¹).^[4–9] According to the value of Tafel slope, the as-prepared N@Mo₂C-3/CFP electrocatalyst, maybe, proceeds via a Volmer–Heyrovsky mechanism, where the electrochemical H_{ads} desorption is the rate-limiting step in an acidic medium.^[9–15] With the ideal amount of N-doping, the Tafel slope value undoubtedly decreases, indicating the improvement of H_{ads} desorption. The exchange current density (*j*₀) is also calculated to evaluate the inherent catalytic activity of the N@Mo₂C-*n*/CFP, obtained from Tafel plots by using the extrapolation methods (see Table S2, Supporting Information). Remarkably, the exchange current density of N@Mo₂C-3/CFP nanosheet is calculated to be 0.42 mA cm⁻², which is also akin to that of 20% Pt/C, indicating its excellent electronic transport efficiency.

Considering the operational stability is another important criterion to evaluate the performance of a HER catalyst, the long-term stability of N@Mo₂C-3/CFP electrocatalyst is further investigated by cycling N@Mo₂C-3/CFP electrode in both acid and basic conditions (Figure 3G,H). After 3000 cyclic voltammetry (CV) cycles, the linear sweep voltammetry profile of the catalyst remains almost unchanged. Meanwhile, chronoamperometry shows a stable hydrogen evolution current–time profile over 20 h in both 0.5 M H₂SO₄ (≈34.3 mA cm⁻² at η = 100 mV; inset of Figure 3G) and 1 M KOH (≈35.2 mA cm⁻² at η = 100 mV; inset of Figure 3H). Additionally, the Faradic efficiency, describing the efficiency with which charge is transferred into the H₂ product, is also studied. The amount of H₂ generated over N@Mo₂C-3/CFP is well consistent with the theoretically value, demonstrating the Faradic efficiency of the N@Mo₂C-3/CFP electrocatalyst is close to 100% in both acid and basic conditions (Figure S10, Supporting Information). After 20 h of electrolysis, the XRD pattern, scanning electron microscopy (SEM), TEM, and HRTEM images of N@Mo₂C-3/CFP reveal that the N@Mo₂C-3/CFP retains its structural integrity (Figure S11, Supporting Information). Thus, N@Mo₂C-3/CFP as a dual medium catalyst shows an excellent catalytic activity and a long-term stability for HER, which presents a benign model for the design of more promising HER electrocatalysts.

To gain more insight into the HER activity of varied N@Mo₂C-*n*/CFP, electrochemical impedance spectroscopy (EIS) is further conducted at an overpotential of 200 mV in 0.5 M H₂SO₄ (Figure S12, Supporting Information). Here a simplified equivalent circuit (inset in Figure S12A, Supporting Information) is employed. Interestingly, N@Mo₂C-3/CFP shows a lowered charge transfer resistance (*R*_{ct}) value (26.15 Ω) than those of the N@Mo₂C-0/CFP (63.35 Ω), N@Mo₂C-1/CFP (53.04 Ω), N@Mo₂C-2/CFP (36.61 Ω), and N@Mo₂C-5/CFP (43.20 Ω). Therefore, it suggests a more efficient electron transport was received at the N@Mo₂C-3/CFP/electrolyte interface due to decreased resistance. Additionally, EIS for N@Mo₂C-3/CFP under different overpotentials is also investigated. As shown in Figure S12B,C (Supporting Information), similar impedance properties at different overpotentials can be seen, suggesting they all hold similar electrochemical processes. Take N@Mo₂C-3/CFP for example, the fitting plot of EIS circuit is also provided in Figure S12D (Supporting Information). The

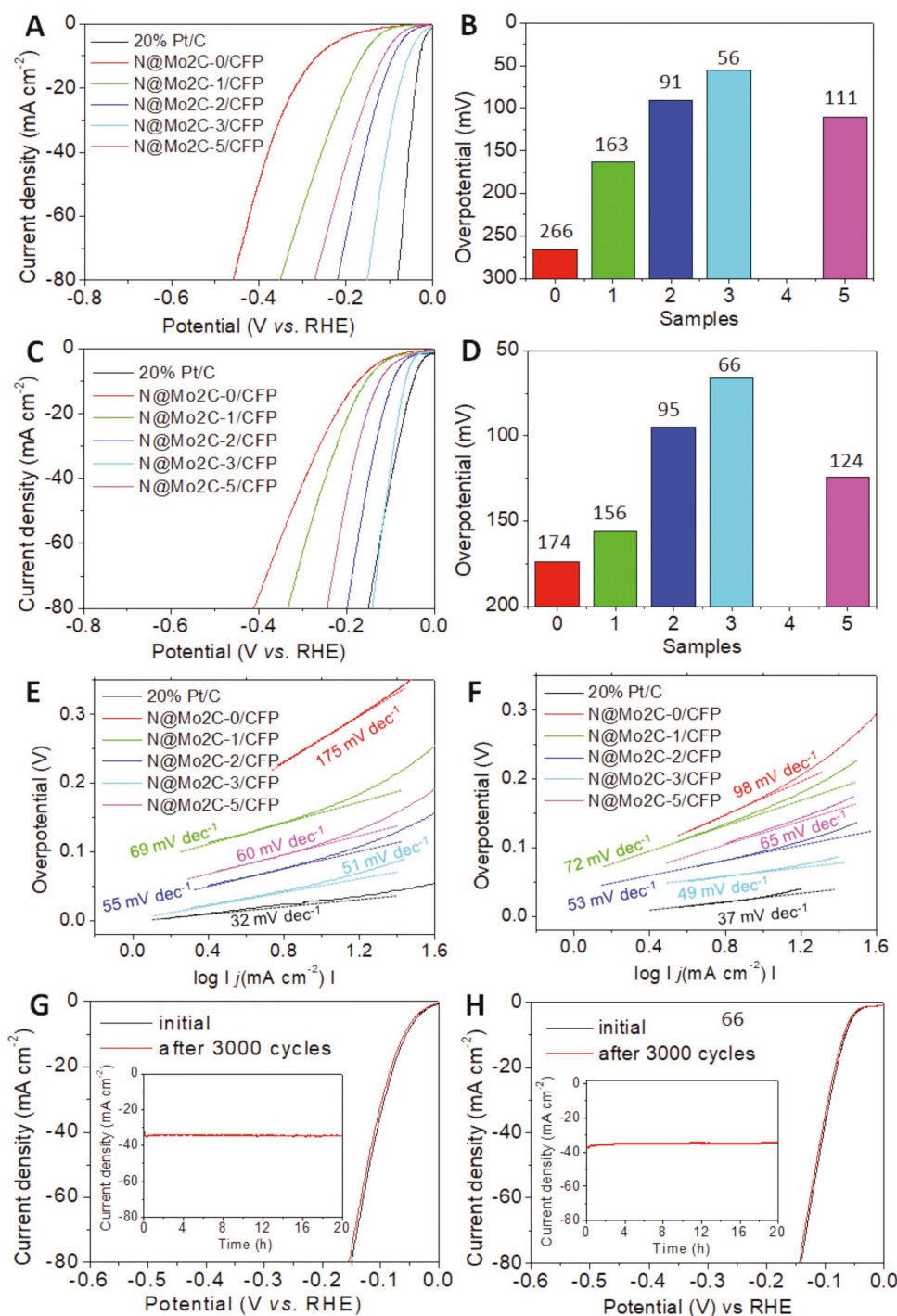


Figure 3. HER performances for varied N@Mo₂C-*n*/CFP electrocatalysts. A) Polarization curve with the same mass loading of 2 mg cm⁻² in 0.5 M H₂SO₄ with a scan rate of 5 mV s⁻¹ under a three-electrode configuration. B) Overpotential of N@Mo₂C-*n*/CFP catalysts at 10 mA cm⁻². C) Tafel plots and D) polarization curve with the same mass loading of 2 mg cm⁻² in 1 M KOH with a scan rate of 5 mV s⁻¹ under a three-electrode configuration. E) Overpotential of N@Mo₂C-*n*/CFP catalysts at 10 mA cm⁻² in 1 M KOH. F) Tafel plots in 1 M KOH. Polarization curve of initial and after 3000 cycles in G) 0.5 M H₂SO₄ and H) 1.0 M KOH. Chronoamperometry *i*-*t* curve of N@Mo₂C-3/CFP electrocatalyst at an overpotential of 100 mV in 0.5 M H₂SO₄ (inset of G) and 1.0 M KOH (inset of H).

plots of overpotential versus logarithmic R_{ct} for various N@Mo₂C-*n*/CFP electrocatalysts are provided in Figure S12E (Supporting Information). It can be seen that R_{ct} decreases with the increase of overpotential for all N@Mo₂C-*n*/CFP

electrocatalysts. Moreover, N@Mo₂C-3/CFP shows the biggest change in log R_{ct} value when the same overpotential change is performed. The slope of N@Mo₂C-3/CFP ($-0.19 \Omega \text{ dec}^{-1}$) has also been demonstrated to be the highest compared with

those of N@Mo₂C-0/CFP (−0.30 Ω dec^{−1}), N@Mo₂C-1/CFP (−0.28 Ω dec^{−1}), N@Mo₂C-2/CFP (−0.22 Ω dec^{−1}), and N@Mo₂C-5/CFP (−0.24 Ω dec^{−1}) (Figure S12E, Supporting Information), indicating its faster charge transfer kinetics. The above results are well consistent with the results of Tafel plots. Moreover, the electrochemical double-layer capacitances (*C_{dl}*) measured by the CV method (Figure S13, Supporting Information) are employed to evaluate the electrochemical surface area (ECSA) of a variety of N@Mo₂C-*n*/CFP electrocatalysts. Remarkably, the *C_{dl}* of N@Mo₂C-*n*/CFP increases from 8.89 to 27.89 mF cm^{−2} with suitable N-doping (Table S2, Supporting Information). Since the *C_{dl}* is proportional to the ECSA, the corresponding *C_{dl}* can be used to identify the difference in electrocatalytic active sites.^[33] Thus, the obviously high *C_{dl}* value of N@Mo₂C-3/CFP (27.89 mF cm^{−2}) indicates the intrinsic optimization of active sites via atomic engineering of suitable N dopants. In order to eliminate the influence of the CFP on HER activity, the HER performance of N@Mo₂C-3/CFP and N@Mo₂C-3 on glassy carbon electrode (N@Mo₂C-3/GCE) and the bare CFP is given in Figure S14 (Supporting Information). The result clearly shows a neglectable activity of the CFP towards hydrogen evolution. However, if CFP support was replaced by GCE, the N@Mo₂C-3/GCE shows decreased activity than N@Mo₂C-3/CFP, implying that a good conductive support like CFP is essential for benign HER performance. Furthermore, the mass loading of N@Mo₂C-3/CFP for the HER has been also optimized (Figures S15 and S16, Supporting Information), suggesting an optimal loading of 2 mg cm^{−2}. We also test the linear sweep voltammetry (LSV) curves of N@Mo₂C-3/CFP with different scan rates (1, 2, and 5 mV s^{−1}), which show no obvious difference between different scan rates (Figure S15c, Supporting Information).

2.4. Interpretation of the Structure–Activity Relationship

We inferred that the high activity and stability of N@Mo₂C-3/CFP stemmed mainly from the atomic-level N-doping-induced chemical structures regulation of Mo₂C. We have probed the chemical nature of varied N@Mo₂C-*n* interfacial layers on CFP using SEM, TEM, and XPS. As shown in Figure 1 and Figure S5 (Supporting Information), the SEM and TEM images of varied N@Mo₂C-*n*/CFP catalysts show that CFP fibers are coated with N@Mo₂C nanoparticles and the nanoparticles sizes on N@Mo₂C-2/CFP (≈20 nm), N@Mo₂C-3/CFP (≈15 nm), and N@Mo₂C-5/CFP (≈10 nm) are smaller than that of N@Mo₂C-0/CFP (≈50 nm) and N@Mo₂C-1/CFP (≈40 nm). Here, one might postulate that the smaller size of the particle is, the higher the HER performance it may endow. However, the features and sizes effects of the nanoparticles on N@Mo₂C-*n*/CFP are not reflected on the HER activity of N@Mo₂C-3/CFP. The N@Mo₂C-3/CFP catalyst with larger nanoparticles (≈50 nm, denoted as N@Mo₂C-3/CFP-50) has been controllably created by applying the initial mass loading (Figure S16, Supporting Information). It can be seen that the HER activity of N@Mo₂C-3/CFP-50 is still superior to that of N@Mo₂C-0/CFP and N@Mo₂C-1/CFP with a size of ≈40–50 nm (Figure S17, Supporting Information), indicating the HER performance of N@Mo₂C-*n*/CFP is reasonably ascribed to their varied

electronic features originated from different amounts of N-doping. Additionally, based on the XPS results, the peaks assignments and percentage of surface Mo–N in varied N@Mo₂C-*n* catalysts are summarized in Table S1b (Supporting Information). It can be seen that surface C–N bonds for N@Mo₂C-0 possess the highest percentage (≈56.2%), whose N sources come from TBA ions in (TBA)₂Mo₆ precursor, indicating the N-doped carbon matrix is mainly derived from TBA ions. It should be noted that the number of TBA ions in each of the (TBA)₂(Mo₆-*n*NAr) precursor is the same (equal to 2). There are two bondings with N, including Mo–N bonds and C–N bonds. As shown in Table S1b (Supporting Information), the percentages of surface Mo–N bonds are raised from 43.8% to 74.5% with the increased amount of N dopants, while the percentages of surface C–N bonds are decreased from 56.2% to 25.5% with the increasing amount of N dopants, indicating the N sources derived from organoimido ligands (Mo–N–Ar) tend to create Mo–N bonds in N@Mo₂C rather than C–N bonds in N-doped carbon matrix during the pyrolysis process. The above XPS results clearly reveal that the electronic structure of Mo atoms in N@Mo₂C-*n* catalysts can be well tuned by the introduction of N atoms (Figure 2E,F), while the amounts of N dopants have little influence on the electronic structure of the carbon matrix (Figure 2E).

DFT calculations were further performed to evaluate the influence of N-doping on Mo–H bonding. The mainly exposed surface in our N@Mo₂C-*n*/CFP electrocatalysts, Mo₂C (1 2 1) (PDF#79-0744), is applied as the model for DFT calculations (Figure 4A; Figures S18–S23, Supporting Information). Theoretically, the HER could be described as a three-state diagram consisting of an initial free H⁺, an intermediate adsorbed H*, and gaseous 1/2 H₂ molecule as the final product. The adsorption free energy of hydrogen, Δ*G_{H*}*, has been widely considered as a useful descriptor for HER catalytic activity.^[23,42] If H binds too weakly to the surface, H⁺ cannot be captured from the dissolved phase, which restrains the HER activity (Volmer step). On the contrary, if H binds too strongly, gaseous H₂ will have difficulty to leave the surface due to an inhibited Heyrovsky/Tafel step. In order to balance the reaction barriers of the H⁺ reduction (Volmer step) and H₂ desorption (Heyrovsky/Tafel steps) to achieve zero overpotential η, one would expect that the optimal catalyst for HER has zero Δ*G_{H*}*.

The free energy diagrams of the HER based on Δ*G_{H*}* over Mo₂C (1 2 1) surface doped with different numbers of N atoms are plotted in Figure 4B. Among the investigated models, pristine Mo₂C (1 2 1) shows the most negative value of Δ*G_{H*}* (−0.50 eV), which represents a strong H adsorption and a low HER activity due to the hindered H₂ desorption (Heyrovsky/Tafel steps). With the increase of N content, the negative Δ*G_{H*}* increases close to zero, which reflects the weakening of Mo–H bonding. As shown in Figure 4B, 3N-Mo₂C (1 2 1) possesses the best Δ*G_{H*}* value of 0.05 eV close to zero, indicating the optimal amount of N incorporation can drive Δ*G_{H*}* values toward zero, leading to the faster kinetics of H_{ads} desorption. However, with excessive N-doping, a positive Δ*G_{H*}* (0.14 eV) for 5N-Mo₂C (1 2 1) can be observed, indicating that the surface bond H strength becomes too weak to capture H⁺, which consequently results in limitation of H⁺ reduction (Volmer step), as confirmed by the Tafel plots (Figure 3C). The theoretical overpotential

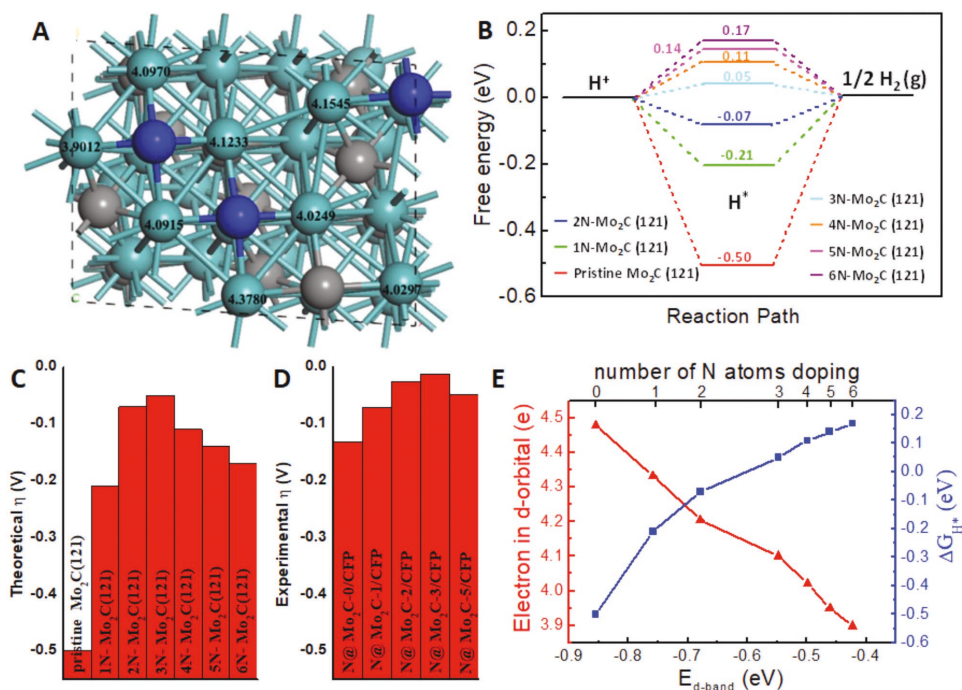


Figure 4. DFT calculation results. A) The top view of 3N-Mo₂C (1 2 1) and valence electron in d-orbital of the surface-exposed Mo atoms. B) The free energy diagram of the HER based on ΔG_{H^*} over the pristine Mo₂C (1 2 1), 1N-doped Mo₂C (1 2 1), 2N-doped Mo₂C (1 2 1), 3N-doped Mo₂C (1 2 1), 4N-doped Mo₂C (1 2 1), 5N-doped Mo₂C (1 2 1), and 6N-doped Mo₂C (1 2 1) surfaces. C) Onset overpotential (η) for HER based on theoretical calculation and D) experiment measurement on different N-doped Mo₂C electrocatalysts. E) The average electron in d-orbital of surface Mo atoms and ΔG_{H^*} versus the d band center of surface Mo atoms ($E_{d\text{-band}}$) on N-doped Mo₂C (1 2 1).

η derived from ΔG_{H^*} is shown in Figure 4C, which is reasonably consistent with the overpotential derived from experiment (Figure 4D). The Mo₂C (1 2 1) with moderated doped N content possesses significantly enhanced catalytic activity for HER, while the excessive introduction of N would impair the catalytic activity, highlighting the importance of controllable atomic engineering of N dopants.

DFT calculations suggest that the volcano-like relationship between η of N-doped Mo₂C (1 2 1) and doped N content can be attributed to the influence of ΔG_{H^*} with the various N-doping amounts. Next, we aim at restoring the doping process from the perspective of configuration transformation of N-doped Mo₂C. As shown in Figure S20 (Supporting Information), N atoms are gradually doped into N-doped Mo₂C (1 2 1) from surface to lattice. Therefore, N atoms would oblige the adjacent adsorbed hydrogen to migrate or even occupy the adsorption sites for hydrogen when it is located at surface interspace (Figure S21, Supporting Information). The root-mean-square displacement (RMSD) of the adsorbed H for N-doped Mo₂C (1 2 1) compared to pristine Mo₂C (1 2 1) as a function of N-doped content is plotted in Figure S22 (Supporting Information). It is found that when the RMSD values increase from 0 Å (pristine Mo₂C (1 2 1) surface) to 1.13 Å (2N-Mo₂C (1 2 1) surface), from the theoretical prediction, the adsorbed hydrogen has to migrate to metastable adsorption sites or even desorb from the surface. From then on, when the increasing amount of N dopants got into the structure, the ΔG_{H^*} value rose up (Figure 4E, Supporting Information). Simultaneously, RMSD value was kept around 1.1 Å with no more evidence of H^{*} displacement

happened (Figure S21, Supporting Information) from 2N-Mo₂C (1 2 1) to 6N-Mo₂C (1 2 1). Therefore, in addition to the steric hindrance effect of N-doping, the influence of N-doping on electronic structure of Mo₂C (1 2 1) is significant. The relationship between the surface adsorption ability of a material and its electronic structure has been explained by many theoretical models, among which d-band center developed by Nørskov and co-workers are applied broadly.^[66] That is, d-orbital occupied by fewer electrons results in a higher location of the d-band center, which yields the bonding states with higher energy level and less occupancy. Eventually, these effects give rise to a weaker interaction between adsorbate and catalyst surface and vice versa. Accordingly, we carried out a Bader charge analysis on valence electron of d-orbital and calculate d-band center by analyzing the projected density of states of all surface-exposed Mo atoms on Mo₂C (1 2 1) doped with different numbers of N atoms (Figure S23, Supporting Information). As presented in Figure 4E, accompanying with the increase of doped N content, a clear shift of d-band center to a higher energy level can be discovered with the decrease of valence electron of d-orbital for surface-exposed Mo atoms (attributed to the higher electronegativity of N than that of Mo) and increased ΔG_{H^*} , which is consistent with d-band center model described above.

3. Conclusion

In summary, a combined theoretical and experimental approach is presented here to facilitate the HER kinetics of

Mo₂C electrocatalysts by fine tuning the electronic structure of Mo₂C electrocatalyst through atomic engineering of nitrogen dopants. For the first time, our observations suggest that N-doping sites in Mo₂C could be well controlled by changing the amount of organoimido ligands in the POM precursors. Moreover, TBA ions as the counterions of POMs could act as an N source for doping in the carbon matrix. The unique structures of organoimido-derivatized POM (TBA)₂(Mo₆-*n*NAr) precursors can reduce the particle aggregation during the high-temperature pyrolysis, since Mo atoms in (TBA)₂Mo₆-*n*NAr are surrounded with organoarylimido ligands by Mo–N bonds and TBA ions via electrostatic interactions, leading to in situ N-doping and homogeneous carburization. The optimized electrocatalyst, N@Mo₂C-3/CFP, showed excellent HER performance and good stability over 20 h under both acidic and basic conditions, superior to that of the ever-reported Mo₂C electrocatalysts. Moreover, the HER performance of the N@Mo₂C-3/CFP catalyst is superior to that of 20% Pt/C when the potential is more negative than –117 mV. The DFT calculations further reveal that moderate substitution of N atoms on carbon sites of Mo₂C is of vital importance for a significant enhancement of HER performance since it can weaken H adsorption strength and promote H_{ad} desorption. Herein, we describe a controllable atomic engineering of nitrogen dopant on Mo₂C by designing organoimido-derivatized POM nanoclusters with inherent Mo–N bonds as precursors, which is able to significantly regulate the electronic structure of Mo₂C towards a great enhancement of HER performance. Therefore, such an effective ligand-controlled atomic engineering strategy may open a new perspective for the design of highly active non-noble catalysts for energy conversions.

4. Experimental Section

Materials and Characterizations: All chemicals, including solvents, were commercially available as the reagent grade from Adamas-beta. Acetonitrile was dried by refluxing in the presence of CaH₂ and was distilled before use. *N,N*-DCC was used directly without further purification. IR spectrum was measured by using KBr pellets and recorded on a Perkin Elmer FT-IR spectrometer. Elemental analyses were performed by Elementar Analysensysteme GmbH (vario EL). PXRD characterization was performed on a Bruker D8 Advance X-ray diffractometer using Cu-Kα radiation ($\lambda = 1.5418 \text{ \AA}$). The morphology and size of the nanostructured products were characterized using a HITACHI H-7700 TEM with an accelerating voltage of 100 kV, and a FEI Tecnai G2 F20 S-Twin HRTEM operating at 200 kV. SEM, with energy dispersive X-ray spectroscopy (EDS) equipment, was performed on a LEO 1530. XPS experiments were carried out on a scanning X-ray microprobe (Quanter SXM, ULVAC-PHI, Inc.) operated at 250 kV, 55 eV with monochromated Al K α radiation. N₂ sorption isotherms were collected on a Micromeritics Tristar 3020 II adsorption analyzer at –196 °C (77 K). BET-specific surface areas were calculated from adsorption data in a relative pressure range from 0.071 to 0.20. The pore size distribution was derived from the adsorption branch of the isotherms. TGA measurements were performed with a Mettler Toledo TGA/SDTA851 in flowing O₂ (50.0 mL min^{–1}) with a heating rate of 20 K min^{–1}. Raman spectra were recorded using a HORIBA JY HR800 confocal Raman microscope employing an Ar-ion laser operating at 633 nm.

Preparation of Mo₆-*n*NAr/CFP Composites: The Mo₆-*n*NAr precursor was synthesized following the published procedures (for details, see the Supporting Information).^[54,60,61,67] Take Mo₆ for example, the as-prepared Mo₆ (0.1 mm) precursor was dissolved in 10 mL anhydrous

acetone to form transparent solutions. CFPs (1 cm × 2 cm) were washed successively with acetone, deionized water, and ethanol three times each with ultrasonic treatment for 30 min before use. Suitable amounts of the above solution (0.1 mol L^{–1}) were carefully dropped on the CFP within the area of 1 cm². The Mo₆/CFP composite was dried at room temperature for 12 h. The preparation of Mo₆-*n*NAr/CFP composites was similar to that of Mo₆/CFP except that Mo₆ was replaced by Mo₆-*n*NAr precursors (including Mo₆-NAr, Mo₆-2NAr, Mo₆-3NAr, Mo₆-5NAr).

Preparation of N@Mo₂C-*n*/CFP Electrocatalysts: The as-prepared Mo₆-*n*NAr/CFP composites were pyrolyzed under argon gas atmosphere at 800 °C for 3 h at a heating rate of 2 °C min^{–1} to give rise to the corresponding N@Mo₂C-*n*/CFP electrocatalysts. The loading amount of the N@Mo₂C-*n* catalysts on CFP was about 2 mg cm^{–2}. For comparison, the electrode containing 2 mg cm^{–2} 20% Pt/C on CFP was prepared as follows: 5 mg of 20% Pt/C powder was dispersed in a 1 mL of solution containing 0.95 mL of ethanol and 50 μL of 0.5 wt% Nafion. The mixture was ultrasonicated for 30 min to generate a homogeneous slurry. Then an appropriate amount of Pt/C slurry was daubed uniformly in 1 cm² of an area on a piece of 1 cm × 2 cm CFP and dried at room temperature for 24 h.

Electrochemical Measurements: All electrochemical tests were conducted with a standard three-electrode system on a CHI660E potentiostat (CH Instruments, China), and all the potentials in this work were referenced to a reversible hydrogen electrode (RHE) according to $E(\text{RHE}) = E(\text{SCE}) + 0.2415 + 0.059 \text{ pH}$, where SCE denotes saturated calomel electrode. The as-prepared N@Mo₂C-*n*/CFP (1 cm × 2 cm) sample was fixed by electrode holder and used as a working electrode. The exposure area of the working electrode could be controlled by adjusting the immersion depth of CFP in the electrolyte. Since both sides of CFP were exposed in the electrolyte, the active area was about 1 cm² when the depth was 0.5 cm. Before the electrochemical tests, the fresh-working electrode was cycled 50 times to stabilize the current, and LSV was tested in 0.5 M H₂SO₄ and 1.0 M KOH, respectively, at a scan rate of 5 mV s^{–1}, and an SCE and graphite rod were used as the reference electrode and counter electrode, respectively. The 95% internal resistance (*i*R) compensation was applied for all LSV measurements unless noted. Additionally, to measure the electrochemical capacitance, CV was obtained from 0.1 to 0.3 V (versus RHE) with sweep rates of 10, 20, 40, 60, 80, and 100 mV s^{–1}, respectively. EIS was performed at various overpotentials with frequency from 0.05 to 10⁶ Hz, respectively, with an AC voltage of 5 mV.

Supporting Information

Supporting Information is available from the Wiley Online Library or from the author.

Acknowledgements

The authors thank Haibing Meng for his help with providing the Raman, BET, and TGA experimenters. Also, the authors thank Kun Chen, Shan She, and Hongli Jia for their help with the discussions and comments on the early versions of this manuscript and providing the precursor experimenters. The authors also thank the financial support by the National Natural Science Foundation of China (NSFC Nos. 91022010, 21631007, 21471087, 21225103, and 21221062), the Specialized Research Fund for the Doctoral Program of Higher Education of China and Tsinghua University Initiative Foundation Research Program (No. 20131089204), SDSU startup funds, the SDSU University Grants Program, and NSF award CEBT-1704992.

Conflict of Interest

The authors declare no conflict of interest.

Keywords

DFT calculations, electrocatalysts, hydrogen evolution, molybdenum carbides, polyoxometalates

Received: March 10, 2018

Revised: May 13, 2018

Published online: June 28, 2018

- [1] J. A. Turner, *Science* **2004**, 305, 972.
- [2] M. S. Dresselhaus, I. L. Thomas, *Nature* **2001**, 414, 332.
- [3] R. Bala Chandran, S. Breen, Y. Shao, S. Ardo, A. Z. Weber, *Energy Environ. Sci.* **2018**, 11, 115.
- [4] L. Barelli, G. Bidini, F. Gallorini, S. Servili, *Energy* **2008**, 33, 554.
- [5] T. E. Mallouk, *Nat. Chem.* **2013**, 5, 362.
- [6] P. Xiao, W. Chen, X. Wang, *Adv. Energy Mater.* **2015**, 5, 1500985.
- [7] Y. Liu, J. Wu, K. P. Hackenberg, J. Zhang, Y. M. Wang, Y. Yang, K. Keyshar, J. Gu, T. Ogitsu, R. Vajtai, J. Lou, P. M. Ajayan, B. C. Wood, B. I. Yakobson, *Nat. Energy* **2017**, 2, 17127.
- [8] X. Zou, Y. Zhang, *Chem. Soc. Rev.* **2015**, 44, 5148.
- [9] D. Voiry, R. Fullon, J. Yang, E. S. C. de Carvalho Castro, R. Kappera, I. Bozkurt, D. Kaplan, M. J. Lagos, P. E. Batson, G. Gupta, A. D. Mohite, L. Dong, D. Er, V. B. Shenoy, T. Asefa, M. Chowalla, *Nat. Mater.* **2016**, 15, 1003.
- [10] C. Canales, F. Varas-Concha, T. E. Mallouk, G. Ramírez, *Appl. Catal. B: Environ.* **2016**, 188, 169.
- [11] G. Li, D. Zhang, Q. Qiao, Y. Yu, D. Peterson, A. Zafar, R. Kumar, S. Curtarolo, F. Hunte, S. Shannon, Y. Zhu, W. Yang, L. Cao, *J. Am. Chem. Soc.* **2016**, 138, 16632.
- [12] Y. P. Zhu, C. Guo, Y. Zheng, S. Z. Qiao, *Acc. Chem. Res.* **2017**, 50, 915.
- [13] Y. Shen, Y. Zhou, D. Wang, X. Wu, J. Li, J. Xi, *Adv. Energy Mater.* **2018**, 8, 1701759.
- [14] H. Park, Y. Zhang, J. P. Scheifers, P. R. Jothi, A. Encinas, B. P. T. Fokwa, *J. Am. Chem. Soc.* **2017**, 139, 12915.
- [15] H. Park, A. Encinas, J. P. Scheifers, Y. Zhang, B. P. T. Fokwa, *Angew. Chem., Int. Ed.* **2017**, 56, 5575.
- [16] S. Jing, L. Zhang, L. Luo, J. Lu, S. Yin, P. K. Shen, P. Tsiakaras, *Appl. Catal. B: Environ.* **2018**, 224, 533.
- [17] M. Miao, J. Pan, T. He, Y. Yan, B. Y. Xia, X. Wang, *Chem. Eur. J.* **2017**, 23, 10947.
- [18] P. Xiao, X. Ge, H. Wang, Z. Liu, A. Fisher, X. Wang, *Adv. Funct. Mater.* **2015**, 25, 1520.
- [19] P. Xiao, Y. Yan, X. Ge, Z. Liu, J.-Y. Wang, X. Wang, *Appl. Catal. B: Environ.* **2014**, 154–155, 232.
- [20] Y. Zhong, X. Xia, F. Shi, J. Zhan, J. Tu, H. J. Fan, *Adv. Sci.* **2016**, 3, 1500286.
- [21] Y. Zhang, B. Ouyang, J. Xu, S. Chen, R. S. Rawat, H. J. Fan, *Adv. Energy Mater.* **2016**, 6, 1600221.
- [22] Z. Luo, R. Miao, T. D. Huan, I. M. Mosa, A. S. Poyraz, W. Zhong, J. E. Cloud, D. A. Kriz, S. Thanneeru, J. He, Y. Zhang, R. Ramprasad, S. L. Suib, *Adv. Energy Mater.* **2016**, 6, 1600528.
- [23] H. Tabassum, W. Guo, W. Meng, A. Mahmood, R. Zhao, Q. Wang, R. Zou, *Adv. Energy Mater.* **2017**, 7, 1601671.
- [24] X.-D. Wang, Y.-F. Xu, H.-S. Rao, W.-J. Xu, H.-Y. Chen, W.-X. Zhang, D.-B. Kuang, C.-Y. Su, *Energy Environ. Sci.* **2016**, 9, 1468.
- [25] T. Tang, W. J. Jiang, S. Niu, N. Liu, H. Luo, Y. Y. Chen, S. F. Jin, F. Gao, L. J. Wan, J. S. Hu, *J. Am. Chem. Soc.* **2017**, 139, 8320.
- [26] N. Kornienko, J. Resasco, N. Becknell, C.-M. Jiang, Y.-S. Liu, K. Nie, X. Sun, J. Guo, S. R. Leone, P. Yang, *J. Am. Chem. Soc.* **2015**, 137, 7448.
- [27] Y.-J. Tang, Y. Wang, X.-L. Wang, S.-L. Li, W. Huang, L.-Z. Dong, C.-H. Liu, Y.-F. Li, Y.-Q. Lan, *Adv. Energy Mater.* **2016**, 6, 1600116.
- [28] X. Zhang, Z. Lai, C. Tan, H. Zhang, *Angew. Chem., Int. Ed.* **2016**, 55, 8816.
- [29] Y. Yan, R. W. Crisp, J. Gu, B. D. Chernomordik, G. F. Pach, A. R. Marshall, J. A. Turner, M. C. Beard, *Nat. Energy* **2017**, 2, 17052.
- [30] J. Gu, J. A. Aguiar, S. Ferrere, K. X. Steirer, Y. Yan, C. Xiao, J. L. Young, M. Al-Jassim, N. R. Neale, J. A. Turner, *Nat. Energy* **2017**, 2, 16192.
- [31] J. R. Kitchin, J. K. Nørskov, M. A. Barteau, J. G. Chen, *Catal. Today* **2005**, 105, 66.
- [32] X. Xu, F. Nosheen, X. Wang, *Chem. Mater.* **2016**, 28, 6313.
- [33] Z. P. Shi, K. Q. Nie, Z. J. Shao, B. X. Gao, H. L. Lin, H. B. Zhang, B. L. Liu, Y. X. Wang, Y. H. Zhang, X. H. Sun, X. M. Cao, P. Hu, Q. S. Gao, Y. Tang, *Energy Environ. Sci.* **2017**, 10, 1262.
- [34] Y.-Y. Ma, C.-X. Wu, X.-J. Feng, H.-Q. Tan, L.-K. Yan, Y. Liu, Z.-H. Kang, E.-B. Wang, Y.-G. Li, *Energy Environ. Sci.* **2017**, 10, 788.
- [35] J. Jia, T. Xiong, L. Zhao, F. Wang, H. Liu, R. Hu, J. Zhou, W. Zhou, S. Chen, *ACS Nano* **2017**, 11, 12509.
- [36] H. Vrubel, X. Hu, *Angew. Chem., Int. Ed.* **2012**, 51, 12703.
- [37] W. X. Chen, J. J. Pei, C. T. He, J. W. Wan, H. L. Ren, Y. Q. Zhu, Y. Wang, J. C. Dong, S. B. Tian, W. C. Cheong, S. Q. Lu, L. R. Zheng, X. S. Zheng, W. S. Yan, Z. B. Zhuang, C. Chen, Q. Peng, D. S. Wang, Y. D. Li, *Angew. Chem., Int. Ed.* **2017**, 56, 16086.
- [38] H. B. Wu, B. Y. Xia, L. Yu, X. Y. Yu, X. W. Lou, *Nat. Commun.* **2015**, 6, 6512.
- [39] J. Zhu, K. Sakaushi, G. Clavel, M. Shalom, M. Antonietti, T. P. Fellinger, *J. Am. Chem. Soc.* **2015**, 137, 5480.
- [40] J. S. Li, Y. Wang, C. H. Liu, S. L. Li, Y. G. Wang, L. Z. Dong, Z. H. Dai, Y. F. Li, Y. Q. Lan, *Nat. Commun.* **2016**, 7, 11204.
- [41] R. Michalsky, Y.-J. Zhang, A. A. Peterson, *ACS Catal.* **2014**, 4, 1274.
- [42] J. Greeley, T. F. Jaramillo, J. Bonde, I. B. Chorkendorff, J. K. Nørskov, *Nat. Mater.* **2006**, 5, 909.
- [43] H. Ang, H. T. Tan, Z. M. Luo, Y. Zhang, Y. Y. Guo, G. Guo, H. Zhang, Q. Yan, *Small* **2015**, 11, 6278.
- [44] R. Ma, Y. Zhou, Y. Chen, P. Li, Q. Liu, J. Wang, *Angew. Chem., Int. Ed.* **2015**, 54, 14723.
- [45] Y. Liu, G. Yu, G.-D. Li, Y. Sun, T. Asefa, W. Chen, X. Zou, *Angew. Chem., Int. Ed.* **2015**, 54, 10752.
- [46] X. Yang, X. Feng, H. Tan, H. Zang, X. Wang, Y. Wang, E. Wang, Y. Li, *J. Mater. Chem. A* **2016**, 4, 3947.
- [47] Y. Y. Chen, Y. Zhang, W. J. Jiang, X. Zhang, Z. Dai, L. J. Wan, J. S. Hu, *ACS Nano* **2016**, 10, 8851.
- [48] D. H. Youn, S. Han, J. Y. Kim, J. Y. Kim, H. Park, S. H. Choi, J. S. Lee, *ACS Nano* **2014**, 8, 5164.
- [49] F. Wang, Y. Sun, Y. He, L. Liu, J. Xu, X. Zhao, G. Yin, L. Zhang, S. Li, Q. Mao, Y. Huang, T. Zhang, B. Liu, *Nano Energy* **2017**, 37, 1.
- [50] X. B. Han, Y. G. Li, Z. M. Zhang, H. Q. Tan, Y. Lu, E. B. Wang, *J. Am. Chem. Soc.* **2015**, 137, 5486.
- [51] H. Lv, J. Song, Y. V. Geletii, J. W. Vickers, J. M. Sumliner, D. G. Musaev, P. Kogerler, P. F. Zhuk, J. Bacsá, G. Zhu, C. L. Hill, *J. Am. Chem. Soc.* **2014**, 136, 9268.
- [52] Q. Yin, J. M. Tan, C. Besson, Y. V. Geletii, D. G. Musaev, A. E. Kuznetsov, Z. Luo, K. I. Hardcastle, C. L. Hill, *Science* **2010**, 328, 342.
- [53] J. Zhang, Y. Huang, G. Li, Y. Wei, *Coordin. Chem. Rev.* **2017**, <https://doi.org/10.1016/j.ccr.2017.10.025>.
- [54] Y. Wei, B. Xu, C. L. Barnes, Z. Peng, *J. Am. Chem. Soc.* **2001**, 123, 4083.
- [55] Y. Huang, J. Zhang, J. Ge, C. Sui, J. Hao, Y. Wei, *Chem. Commun.* **2017**, 53, 2551.
- [56] Y. Huang, J. Zhang, J. Hao, Y. Wei, *Sci. Rep.* **2016**, 6, 24759.
- [57] Y. Huang, J. Ge, J. Hu, J. Zhang, J. Hao, Y. Wei, *Adv. Energy Mater.* **2018**, 8, 1701601.
- [58] T. Wu, M. Pi, D. Zhang, S. Chen, *J. Power Sources* **2017**, 351, 51.
- [59] Y. Holade, D. P. Hickey, S. D. Minteer, *J. Mater. Chem. A* **2016**, 4, 17154.

- [60] Y. Xia, Y. Wei, Y. Wang, H. Guo, *Inorg. Chem.* **2005**, *44*, 9823.
- [61] J. Hao, Y. Xia, L. Wang, L. Ruhlmann, Y. Zhu, Q. Li, P. Yin, Y. Wei, H. Guo, *Angew. Chem., Int. Ed.* **2008**, *47*, 2626.
- [62] A. Y. Lee, D. M. Blakeslee, C. J. Powell, J. R. Rumble, *Data Sci. J.* **2006**, *1*, 1.
- [63] L. Ramqvist, K. Hamrin, G. Johansson, A. Fahlman, C. Nordling, *J. Phys. Chem. Solids* **1969**, *30*, 1835.
- [64] L. Leclercq, M. Provost, H. Pastor, J. Grimblot, A. M. Hardy, L. Gengembre, G. Leclercq, *J. Catal.* **1989**, *117*, 371.
- [65] H. Lin, N. Liu, Z. Shi, Y. Guo, Y. Tang, Q. Gao, *Adv. Funct. Mater.* **2016**, *26*, 5590.
- [66] T. Bligaard, J. K. Nørskov, *Chemical Bonding at Surfaces and Interfaces* (Eds: A. Nilsson, L. G. M. Pettersson, J. K. Nørskov), Elsevier, Amsterdam **2008**.
- [67] W. G. Klemperer, *Inorg. Synth.* **1990**, *27*, 74.